

Ultrasensitive nonlinear measurements of femtosecond pulses in the telecommunications band by aperiodically poled LiNbO₃ waveguides

Shang-Da Yang,^{1,2,*} Houxun Miao,² Zhi Jiang,² Andrew M. Weiner,² Krishnan R. Parameswaran,³ and Martin M. Fejer³

¹National Tsing Hua University, Hsinchu 30013, Taiwan

²Purdue University, West Lafayette, Indiana 47907, USA

³E. L. Ginzton Laboratory, Stanford University, Stanford, California 94305, USA

*Corresponding author: shangda@ee.nthu.edu.tw

Received 15 May 2007; revised 22 July 2007; accepted 22 July 2007;
posted 24 July 2007 (Doc. ID 82776); published 12 September 2007

We have used aperiodically poled lithium niobate waveguides to perform intensity autocorrelation and frequency-resolved optical gating (FROG) measurements for ultraweak femtosecond pulses at 1.5 μm wavelength. The required pulse energies for intensity autocorrelation and FROG are as low as 52 aJ and 124 aJ, respectively. The corresponding sensitivities are $3.2 \times 10^{-7} \text{ mW}^2$ and $2.7 \times 10^{-6} \text{ mW}^2$, about 3–5 orders of magnitude better than the previous records. The high nonlinear conversion efficiency is attributed to the long waveguide structure, and the needed broad phase-matching bandwidth is realized by chirping the poling period. We discuss the theory of intensity autocorrelation and FROG measurements in the presence of different phase-matching bandwidths, and we show, for the first time to our knowledge, that the distorted intensity autocorrelation trace due to a δ -like phase-matching spectrum is described by a modified field autocorrelation function. We also report new experimental results comparing autocorrelation traces measured with chirped and unchirped waveguide samples and demonstrating high-quality FROG measurements for cubic phase waveforms generated in a programmable pulse shaper. © 2007 Optical Society of America

OCIS codes: 320.7100, 190.7110, 130.3730, 120.3180.

1. Introduction

The versatile applications of ultrafast optics rely largely on the capability of characterizing ultrashort (<1 ps) signal pulses. This is especially true when nearly chirp-free or precisely shaped pulses are involved, such as those in the high bit-rate telecommunication transmissions [1], coherently controlled two-photon fluorescence microscopy [2], optical code-division multiple-access systems [3], and nonlinear-optical material characterizations [4]. Since the time scale of interest is much faster than any existing photodetector, optical gating schemes are required to measure ultrashort pulses. Nonlinear-optical interactions, such as second-harmonic generation (SHG), two-

photon absorption, and four-wave mixing, have been widely used in nonlinear gating for femtosecond pulse measurements. The sensitivity of these nonlinear techniques, however, is usually low and generally does not meet the requirements of low (submicrowatt) average powers for optical communication system monitoring [5] or low (subfemtojoule) signal pulse energies for material characterizations [6]. For high-speed telecommunications, iterative pulse retrieval from linear spectrograms obtained by long (~30 ps) electronic gating has been demonstrated to be capable of measuring relatively short (>2.7 ps) optical pulses [7]. This linear technique, however, remains inapplicable in the femtosecond regime and requires high-speed (>10 GHz) electronics even in measuring pulse trains of low repetition rates.

Several sensitive schemes have been proposed to characterize ultraweak ultrashort optical pulses.

0003-6935/07/276759-11\$15.00/0

© 2007 Optical Society of America

The temporal analysis by dispersing a pair of light electric fields (TADPOLE) technique was demonstrated to measure near-infrared pulses of 42 zJ (42×10^{-21} J) per shot [6]. Optical parametric amplification cross-correlation FROG permits measurement of sliced white-light continuum pulses around 600-nm wavelength at 50 aJ (50×10^{-18} J) [8]. These techniques have two major limitations. First, they require synchronized reference pulses with predetermined intensity/phase profiles and a temporal duration shorter than that of the unknown pulses. In some important cases, such as characterization of pulses at the intermediate or receiving ends of an optical communication link, the required reference is often unavailable. Second, the overall power requirement is actually limited by the sensitivity of the reference-free method employed to fully characterize the reference pulse (which requires much higher energy). Consequently, it is important to improve the measurement sensitivity of self-referenced schemes.

Intensity autocorrelation and FROG [9] using SHG in bulk crystals are standard techniques in characterizing pulse durations and intensity/phase profiles of ultrashort pulses in the absence of a reference. However, the nonlinear conversion efficiency is restricted in part by diffraction, which prohibits the coexistence of a small beam cross section and a long interaction length. When ultrashort pulses are involved, the broad input spectrum should be phase matched to avoid distortion of intensity autocorrelation traces [10] and spectral truncation in FROG spectrograms [9]. Since the phase-matching (PM) bandwidth is inversely proportional to the group velocity mismatch (GVM) walkoff (which is the product of interaction length and GVM between fundamental and second-harmonic waves), thin nonlinear crystals are typically employed (e.g., thickness of LiNbO_3 should be less than 1 mm when measuring 300-fs pulses at 1.5- μm wavelength), further limiting the conversion efficiency. As a result, SHG bulk crystals only offer quadratic sensitivities (defined as the minimum peak-power average-power product needed to generate a detectable nonlinear signal) of $\sim 1 \text{ mW}^2$ for intensity autocorrelation and $\sim 500 \text{ mW}^2$ for FROG, respectively [11,1].

Much effort has been paid to improve the sensitivities of intensity autocorrelation and FROG measurements. Several recent intensity autocorrelation experiments at 1.5- μm wavelength exploited broadband two-photon absorption in silicon avalanche photodiodes [12], GaAs photomultiplier tubes [13], and InGaAsP laser diodes [14]. Measurement sensitivity as low as $1.5 \times 10^{-4} \text{ mW}^2$ has been reported [14], which is about 4 orders of magnitude better than that achieved by conventional SHG bulk crystals. On the other hand, four-wave mixing in a semiconductor optical amplifier and in a spool of 22-km-long dispersion-shifted fiber were used to demonstrate quadratic FROG measurements with sensitivities of 50 mW^2 and 0.2 mW^2 , respectively [15,16]; improving on the conventional SHG FROG scheme using bulk

crystals by 1–3 orders of magnitude. Despite the impressive progress, the resulting sensitivities of these two-photon absorption and four-wave mixing approaches still do not meet the requirement for sub-microwatt average powers for 10-Gbit/s optical communication system monitoring [5].

In this paper, we report on record sensitivities for intensity autocorrelation and FROG measurements by using long aperiodically poled LiNbO_3 (A-PPLN) waveguides. Section 2 examines the fundamentals of pulsed SHG, autocorrelation, and FROG measurements when different PM bandwidths are present. As a special case of the theory published in Ref. [10], an analytical description of the distortion introduced into the intensity autocorrelation trace in the limit of extremely narrow PM bandwidth is derived for the first time to our knowledge. Section 3 elucidates how to engineer the phase-matching response by chirping and apodization of quasi-phase matched (QPM) gratings, as well as the details of our A-PPLN waveguide device used in the experiments. In Section 4 we report a series of experimental results of intensity autocorrelation and FROG measurements. Our data demonstrate record sensitivities of $3.2 \times 10^{-7} \text{ mW}^2$ for intensity autocorrelation [17] and $2.7 \times 10^{-6} \text{ mW}^2$ for FROG [18], improving upon previous sensitivities [14,16] by 500 and 750,000 times, respectively. In addition, we report previously unpublished experimental results comparing autocorrelation traces measured with chirped and unchirped waveguide samples and demonstrating FROG measurements for cubic phase waveforms generated in a programmable pulse shaper. These data clearly illustrate the importance of adequate PM bandwidth and demonstrate the possibility of high quality waveform retrieval with pulses of greater complexity than in our previous experiments. In Section 5 we conclude and discuss some ideas for future improvements.

2. Theory of Nonlinear Pulse Measurements

Femtosecond pulse measurement usually relies on a nonlinear process to perform ultrafast optical gating. SHG is the most widely employed process, especially for measurements with femtosecond oscillators, because it is more efficient than processes using $\chi^{(3)}$. In this section we summarize the theory of SHG for short pulses under the low-conversion condition. It can be used to formulate intensity autocorrelation and FROG measurements by introducing a variable time delay in the presence of a Michelson interferometer. The influence of finite PM bandwidth on pulsed SHG and especially on pulse measurements is analyzed to justify the employment of chirped QPM devices for accurate pulse characterization.

A. Theory of Pulsed Second Harmonic Generation

Given the sinusoidal wave at angular frequency ω_0 is nondepleted and perfectly phase matched [i.e., wavevector mismatch $\Delta k \equiv k_{2\omega_0} - 2k_{\omega_0} = k(2\omega_0) - 2k(\omega_0) = 0$], the output second-harmonic (SH) inten-

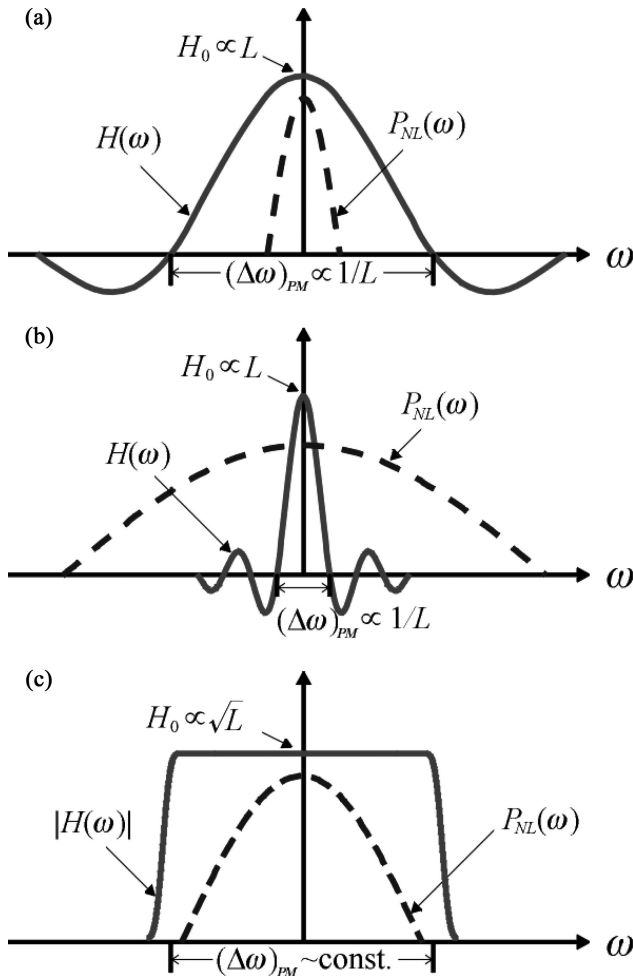


Fig. 1. Spectral representation of SHG using (a) thin crystal of broad PM bandwidth, (b) thick crystal of narrow PM bandwidth, and (c) thick engineered crystal with broadened PM bandwidth.

sity $I_{2\omega}$ due to nonlinear interaction of fundamental intensity I_ω over a length L becomes $I_{2\omega} = \Gamma^2 L^2 I_\omega^2$, where $\Gamma^2 \approx 2\omega_0^2 d_{\text{eff}}^2 / \varepsilon_0 c^3 n^3$, d_{eff} is the effective nonlinear coefficient, n is refractive index, and c and ε_0 are light speed and permittivity in vacuum, respectively [19,20]. As a result, the SHG efficiency normalized to input fundamental power $I_{2\omega}/[I_\omega \langle P_\omega \rangle]$ is typically used as a figure of merit (with units of %/W) for continuous-wave second-harmonic converters. In the presence of short pulses, the SHG formalism can be simplified by assuming (i) a nondepleted pump, (ii) perfect phase matching at the center frequencies, (iii) the fundamental pulse satisfies the slowly varying envelope approximation, and (iv) group velocity dispersion (GVD) is negligible. This will result in an equation relating the spectral amplitudes (Fourier transform of temporal envelopes) of SH and fundamental pulses [10,19,20]:

$$A_{2\omega}(L, \omega) = -j\kappa P_{\text{NL}}(\omega) \times H(\omega), \quad (1)$$

where $\kappa \equiv \omega_0/[n(2\omega_0)c]$, $P_{\text{NL}}(\omega) \equiv A_\omega(\omega) \otimes A_\omega(\omega)$ (\otimes denotes convolution) is the nonlinear polarization

spectrum due to the fundamental pulse, and $H(\omega)$ is the phase-matching spectrum provided by the nonlinear crystal. If the effective nonlinear coefficient d_{eff} is constant across the crystal, we have

$$H(\omega) = d_{\text{eff}} L \times \text{sinc}(T_s \omega / 2), \quad (2)$$

where $\text{sinc}(x) \equiv \sin(x)/x$, $T_s \equiv \Delta(v_g^{-1}) \times L$ is the walkoff arising from group velocity mismatch, and $\Delta(v_g^{-1}) \equiv k'(2\omega_0) - k'(\omega_0)$ (prime notation represents first-order derivative). The PM bandwidth, defined as the full width at half-maximum (FWHM) of the phase-matching power spectrum, would be $(\Delta\omega)_{\text{PM}} \approx 5.57/T_s$ and $(\Delta\nu)_{\text{PM}} \approx 0.886/T_s$. As is shown in Section 3, the corresponding phase-matching tuning curve has an FWHM $(\Delta\lambda)_{\text{PM}} \approx 0.443\lambda_0/(\nu_0 T_s)$, where λ_0 is the central wavelength of the fundamental pulse, and $\nu_0 = c/\lambda_0$. The SH pulse energy $U_{2\omega}$ is proportional to the integration of power spectrum $|A_{2\omega}(L, \omega)|^2$:

$$U_{2\omega} \propto \int_{-\infty}^{\infty} |P_{\text{NL}}(\omega)|^2 \times |H(\omega)|^2 d\omega. \quad (3)$$

We examine the influence of the phase-matching spectrum on the waveform and energy of SH pulse by three special cases illustrated in Fig. 1.

1. Thin Crystal with Broad Phase-Matching Bandwidth

As shown in Fig. 1(a), $P_{\text{NL}}(\omega)$ only overlaps with a small portion of $H(\omega)$, where $H(\omega) \approx d_{\text{eff}} L$:

$$A_{2\omega}(L, \omega) \approx -j\kappa d_{\text{eff}} L \times P_{\text{NL}}(\omega). \quad (4)$$

The SH field and intensity envelopes are proportional to the square of their fundamental counterparts: $a_{2\omega}(L, t) \propto a_\omega^2(t)$, $I_{2\omega}(L, t) = \Gamma^2 L^2 I_\omega^2(t)$. The average SH power (defined as $U_{2\omega}/T_{\text{rep}}$, T_{rep} is the repetition period) becomes $\langle P_{2\omega} \rangle = \Gamma^2 (L^2/A_{\text{eff}}) \times [\hat{P}_\omega \langle P_\omega \rangle]$, where A_{eff} denotes the effective cross-sectional area for both fundamental and second-harmonic beams, and \hat{P}_ω represents the peak fundamental power [20]. This relation indicates the following: (i) The SHG efficiency normalized to peak fundamental power $\langle P_{2\omega} \rangle / [\langle P_\omega \rangle \hat{P}_\omega]$ is a figure of merit (with units of %/W) of “quasi-continuous wave” second-harmonic converters. (ii) The higher the efficiency of the second-harmonic converter, the lower the value of $[\hat{P}_\omega \langle P_\omega \rangle]$ needed to generate a detectable average SH power $\langle P_{2\omega} \rangle$ (for a given detector sensitivity at second-harmonic band and integration time). Consequently, we normally use the expression

$$S \equiv \hat{P}_\omega \times \langle P_\omega \rangle \quad (5)$$

to estimate the sensitivity of quadratic pulse measurement schemes.

2. Thick Crystal with Narrow Phase-Matching Bandwidth

Figure 1(b) shows the case where the SH spectrum is dominated by $H(\omega)$, while $P_{NL}(\omega)$ is approximated by $P_{NL}(0)$:

$$A_{2\omega}(L, \omega) \approx -jk d_{\text{eff}} L P_{NL}(0) \times \text{sinc}[T_s \omega / 2]. \quad (6)$$

Equation (6) corresponds to a square pulse of duration T_s in the time domain: $a_{2\omega}(L, t)$, $I_{2\omega}(L, t) \propto \Pi(t/T_s)$, where $\Pi(x) \equiv \{1, \text{ for } |x| \leq 1/2; 0, \text{ otherwise}\}$. The fundamental field $a_\omega(t)$ contributes to the SH pulse energy via $P_{NL}(0) = \int_{-\infty}^{\infty} a_\omega^2(t) dt$. If the fundamental pulse is free of phase modulation [$a_\omega(t)$ is real], the average SH power becomes $\langle P_{2\omega} \rangle \propto (L/A_{\text{eff}}) \times [U_\omega \langle P_\omega \rangle]$. This relation reveals some unique features of SHG with fundamental spectra much broader than the PM bandwidth: (i) SHG efficiency normalized to fundamental pulse energy $\langle P_{2\omega} \rangle / [\langle P_\omega \rangle U_\omega]$ should be a figure of merit (with units of %/J) for second-harmonic converters; (ii) Eq. (5) is an improper metric to evaluate measurement sensitivity; (iii) the second-harmonic yield scales with L , instead L^2 .

3. Thick Engineered Crystal with Broadened Phase-Matching Bandwidth

As is discussed in Subsection 3.A, proper design of nonlinear coefficient distribution $d_{\text{eff}}(z)$ can broaden the PM bandwidth of thick crystals to span the region of significant $P_{NL}(\omega)$ [see Fig. 1(c)]. In the absence of amplitude modulation of $|d_{\text{eff}}(z)|$, the phase-matching power spectral area $A_{\text{PM}} \equiv \int_{-\infty}^{\infty} |H(\omega)|^2 d\omega$ (i.e., available nonlinearity) still scales with crystal length L , making $|H(\omega)| \propto \sqrt{L}$ in the transparent band of a rectangular phase-matching response and leading to

$$A_{2\omega}(L, \omega) \propto \sqrt{L} P_{NL}(\omega) \times \exp[j\angle H(\omega)]. \quad (7)$$

The SH pulse could be substantially broader than $a_\omega^2(t)$ if the phase-matching spectral phase $\angle H(\omega)$ is highly nonlinear. However, the SH energy and power spectrum is independent of $\angle H(\omega)$. The average SH power satisfies $\langle P_{2\omega} \rangle \propto (L/A_{\text{eff}}) \times [\hat{P}_\omega \langle P_\omega \rangle]$, corresponding to features lying between those of two previous cases: (i) $\langle P_{2\omega} \rangle / [\langle P_\omega \rangle \hat{P}_\omega]$, and Eq. (5) remain appropriate to characterize second-harmonic converters and measurement sensitivity, respectively. (ii) The second-harmonic yield scales with L .

B. Theory of Autocorrelation Measurements

Intensity autocorrelation measurement is widely used to estimate ultrashort pulse duration. Here we compare the analytic formulas of the autocorrelation traces obtained by broadband and narrowband SHG crystals, respectively.

1. Intensity Autocorrelation with Broad Phase-Matching Bandwidth [9,20,21]

Figure 2 illustrates the collinear geometry of intensity autocorrelation measurement. The Michelson in-

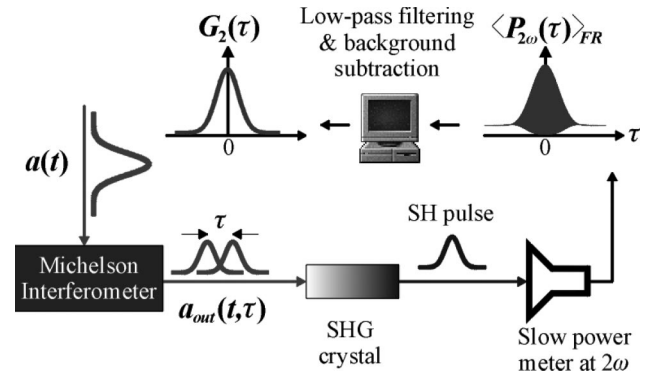


Fig. 2. Collinear geometry of intensity autocorrelation measurement.

terferometer splits and recombines the input pulse of field envelope $a(t)$ to produce a pulse pair: $a_{\text{out}}(t, \tau) = a(t) + a(t - \tau)e^{-j\omega_0\tau}$. By Eqs. (4) and (7), the second-harmonic yield due to broadband SHG crystals [such as those in Figs. 1(a) and 1(c)] should be $\langle P_{2\omega} \rangle \propto \int_{-\infty}^{\infty} |P_{NL}(\omega)|^2 d\omega \propto \int_{-\infty}^{\infty} |a_\omega^2(t)|^2 dt$. By substituting $a_\omega(t) = a_{\text{out}}(t, \tau)$, we obtain a fringe-resolved autocorrelation trace $\langle P_{2\omega}(\tau) \rangle_{\text{FR}}$ measurable by a slow powermeter sensitive at the second-harmonic band. The interferometric fringes can be removed by low-pass filtering, leading to a trace $\langle P_{2\omega}(\tau) \rangle \propto 1 + 2G_2(\tau)$, where

$$G_2(\tau) \equiv \langle I(t)I(t - \tau) \rangle / \langle I^2(t) \rangle \quad (8)$$

is the normalized intensity autocorrelation function [$I(t) \equiv |a(t)|^2$, $\langle \rangle$ represents time average]. For well-behaved pulse shapes, the pulse width Δt can be roughly estimated by deconvolution of the correlation width $\Delta\tau$ of $G_2(\tau)$. Nevertheless, $G_2(\tau)$ only delivers very limited pulse information for lack of the spectral phase of intensity profile $I(t)$ [20,21].

2. Distortion of Autocorrelation due to Narrow Phase-Matching Bandwidth

The distortion of intensity autocorrelation measurement due to insufficient PM bandwidth has been formulated and numerically investigated in Ref. [10]. An important limit is the case of a very narrow phase-matching spectrum $H(\omega)$, which we derive here for the first time to our knowledge. For a δ -like phase-matching spectrum, Eqs. (3) and (6) result in $\langle P_{2\omega} \rangle \propto |P_{NL}(0)|^2 [P_{NL}(0) = \int_{-\infty}^{\infty} a_\omega^2(t) dt]$. Substituting $a_\omega(t) = a_{\text{out}}(t, \tau)$ makes $P_{NL}(0) = 2[\int_{-\infty}^{\infty} a^2(t) dt] \times e^{-j\omega_0\tau} \times [G_1'(\tau) + \cos(\omega_0\tau)]$, where

$$G_1'(\tau) \equiv \langle a(t)a(t - \tau) \rangle / \langle a^2(t) \rangle \quad (9)$$

is defined as the modified field autocorrelation function (different from the conventional field autocorrelation function $\Gamma(\tau) \equiv \langle a(t)a^*(t - \tau) \rangle / \langle |a(t)|^2 \rangle$). The fringe-resolved and fringe-free autocorrelation traces obtained in the case of a δ -like phase-matching spectrum are

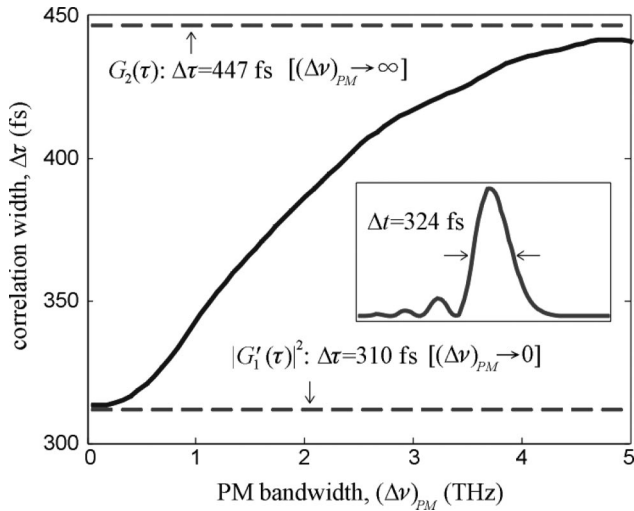


Fig. 3. Simulated correlation width (FWHM) versus PM bandwidth for a nonlinearly chirped Gaussian pulse. The inset shows the intensity profile of the pulse.

$$\begin{aligned} \langle P_{2\omega}(\tau) \rangle_{\text{FR}} &\propto 1 + 2|G_1'(\tau)|^2 + 4\text{Re}\{G_1'(\tau)\}\cos(\omega_0\tau) \\ &\quad + \cos(2\omega_0\tau), \\ \langle P_{2\omega}(\tau) \rangle &\propto 1 + 2|G_1'(\tau)|^2, \end{aligned} \quad (10)$$

respectively. In general, $|G_1'(\tau)|^2 \neq G_2(\tau)$ except for some special pulse shapes [10]. This difference remains even if $a(t)$ is real, since generally $[\int a(t)a(t-\tau)dt]^2 \neq \int a^2(t)a^2(t-\tau)dt$. The difference becomes larger for chirped pulses, because $|G_1'(\tau)|^2$ is sensitive to the phase of $a(t)$. Figure 3 illustrates the simulated correlation width $\Delta\tau$ (FWHM) of a nonlinearly chirped Gaussian pulse as a function of PM bandwidth $(\Delta\nu)_{\text{PM}}$. The spectral amplitude is assumed as $A(\nu) = \exp[-(\nu/1.7 \text{ THz})^2 + j\pi(\nu/\Delta\nu)^3]$, where $|A(\nu)|^2$ has an FWHM of $\Delta\nu = 2 \text{ THz}$, corresponding to an asymmetric intensity profile with FWHM $\Delta t = 324 \text{ fs}$ (see inset). For simplicity, we assume rectangular phase-matching spectra with different full widths $(\Delta\nu)_{\text{PM}}$. The correlation width increases from 310 fs to 447 fs as $(\Delta\nu)_{\text{PM}}$ increases from 0 to ∞ . The minimum PM bandwidth needed to approximately obtain standard $G_2(\tau)$ depends on the bandwidth $\Delta\nu$ and chirp of the input pulse. A rule of thumb is $(\Delta\nu)_{\text{PM}} > 2\Delta\nu$ for pulses without strong chirp. In addition to purely theoretical interests, measuring fringe-resolved trace $\langle P_{2\omega}(\tau) \rangle_{\text{FR}}$ caused by a δ -like phase-matching spectrum $H(\omega)$ could be useful in retrieving spectral phase information of the pulse [22]. This is partly due to each frequency component of the nonlinear polarization spectrum $P_{\text{NL}}(\omega)$ being associated with the entire fundamental spectrum $A_\omega(\omega)$ through autoconvolution, and spectral “sampling” by a narrow $H(\omega)$ at second-harmonic band [Eq. (6)] still preserves significant pulse information.

C. Theory of Interferometric Second Harmonic Generation Frequency-Resolved Optical Gating SHG FROG [8] provides complete amplitude and phase information without the need of synchronized

reference or monochromatic pump as required in Refs. [14,15,23]. It applies the strategy of (i) using the unknown pulse itself for ultrafast gating, (ii) recording considerably more data points compared to the degrees of freedom, and (iii) then retrieving the complex field by iteration. SHG FROG is relatively robust against systematic error and noise contamination due to self-contained consistency checks. The sensitivity of conventional SHG FROG using thin bulk crystals, however, is limited by $\sim 500 \text{ mW}^2$ [1]. This number can be greatly improved by using A-PPLN waveguides [18] if the problems of interferometric fringes and spectral distortion in FROG traces can be alleviated. Here we summarize the formalism of interferometric SHG FROG [24] and describe our solutions to the technical difficulties.

The standard FROG trace typically obtained by noncollinear SHG is defined as

$$I_{\text{FROG}}(\omega, \tau) \equiv |F_t\{a(t) \times a(t-\tau)\}|^2 = |P_{\text{NL}}^X(\omega, \tau)|^2, \quad (11)$$

where $F_t\{\}$ denotes Fourier transform with respect to variable t , and $P_{\text{NL}}^X(\omega, \tau) \equiv F_t\{a(t) \times a(t-\tau)\}$ is the self-gated nonlinear polarization spectrum. Since our straight A-PPLN waveguides can only work with collinear geometry and guide only transverse magnetic (TM) polarization mode, we have to employ a collinear Michelson interferometer that yields interferometric FROG traces (Fig. 4). The nonlinear polarization caused by the collinear pulse pair becomes $P_{\text{NL}}(t, \tau) = [a(t) + a(t-\tau) \times \exp(-j\omega_0\tau)]^2$, corresponding to a spectrum of

$$\begin{aligned} P_{\text{NL}}(\omega, \tau) &= P_{\text{NL}}^X(\omega, 0) \times \{1 + e^{-j(2\omega_0+\omega)\tau}\} \\ &\quad + 2P_{\text{NL}}^X(\omega, \tau) \times e^{-j\omega_0\tau}. \end{aligned}$$

Ideal broadband SHG results in fringe-resolved FROG trace $I_{\text{FR}}(\omega, \tau)$ proportional to $|P_{\text{NL}}(\omega, \tau)|^2$:

$$\begin{aligned} I_{\text{FR}}(\omega, \tau) &\propto I_{\text{FROG}}(\omega, 0) + 2I_{\text{FROG}}(\omega, \tau) \\ &\quad + 4\sqrt{I_{\text{FROG}}(\omega, 0) \times I_{\text{FROG}}(\omega, \tau)} \\ &\quad \times \cos(\Delta\psi + \omega\tau/2) \times \cos[(\omega_0 + \omega/2)\tau] \\ &\quad + I_{\text{FROG}}(\omega, 0) \times \cos[(2\omega_0 + \omega)\tau], \end{aligned} \quad (12)$$

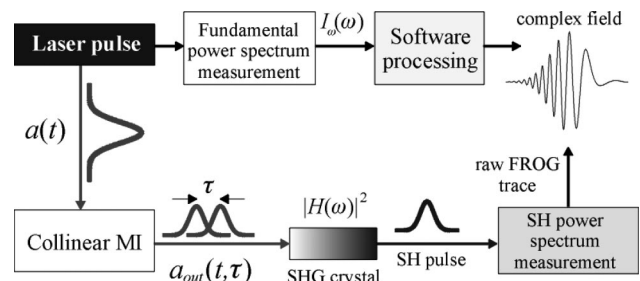


Fig. 4. Schematic of interferometric SHG FROG measurement. MI, Michelson interferometer.

where $\Delta\psi \equiv \angle P_{\text{NL}}^X(\omega, \tau) - \angle P_{\text{NL}}^X(\omega, 0)$. The Fourier transform of Eq. (12) [defined as $\int_{-\infty}^{\infty} I_{\text{FR}}(\omega, \tau) e^{-j\Omega\tau} d\tau$] shows five spectral strips centered at delay frequencies of $\Omega = 0, \pm\omega_0$, and $\pm 2\omega_0$, respectively. The fringe-free trace can be derived by low-pass filtering: $I_{\text{LPF}}(\omega, \tau) = I_{\text{FROG}}(\omega, 0) + 2I_{\text{FROG}}(\omega, \tau)$.

In practice, the phase-matching power spectrum $|H(\omega)|^2$ of our A-PPLN waveguides exhibits considerable fluctuation (see Section 3) and can distort the measured traces: $\tilde{I}_{\text{FR}}(\omega, \tau) = I_{\text{FR}}(\omega, \tau) \times |H(\omega)|^2$,

$$\tilde{I}_{\text{LPF}}(\omega, \tau) = [I_{\text{FROG}}(\omega, 0) + 2I_{\text{FROG}}(\omega, \tau)] \times |H(\omega)|^2. \quad (13)$$

Since $I_{\text{FROG}}(\omega, \tau) \rightarrow 0$ when $|\tau|$ is much greater than the pulse width Δt , we can eliminate the signal background of Eq. (13) by subtracting a spectral slice taken at large delay: $\tilde{I}_{\text{FROG}}(\omega, \tau) \propto I_{\text{FROG}}(\omega, \tau) \times |H(\omega)|^2$. Instead of directly measuring $|H(\omega)|^2$ by using a tunable monochromatic source (which is subject to environmental perturbations that in our experiments hindered sufficiently accurate determination of $|H(\omega)|^2$), we can retrieve it by the frequency marginal correction method [25]. The ideal frequency marginal function $M(\omega)$, defined as the delay integral of the standard FROG trace, is equivalent to the autoconvolution of fundamental power spectrum $I_\omega(\omega)$: $M(\omega) \equiv \int_{-\infty}^{\infty} I_{\text{FROG}}(\omega, \tau) d\tau = I_\omega(\omega) \otimes I_\omega(\omega)$. In the presence of a τ -independent spectral modulation $|H(\omega)|^2$, it changes to $\tilde{M}(\omega) \equiv \int_{-\infty}^{\infty} \tilde{I}_{\text{FROG}}(\omega, \tau) d\tau = M(\omega) \times |H(\omega)|^2$, leading to the relation

$$|H(\omega)|^2 = \left[\int_{-\infty}^{\infty} \tilde{I}_{\text{FROG}}(\omega, \tau) d\tau \right] / [I_\omega(\omega) \otimes I_\omega(\omega)]. \quad (14)$$

Equation (14) shows that the FROG data contain useful information about $|H(\omega)|^2$, and we only need to measure fundamental power spectrum $I_\omega(\omega)$ by an optical spectrum analyzer (OSA). Furthermore, $|H(\omega)|^2$ in Eq. (14) can characterize the overall spectral distortion of the measurement system (not limited to that arising from phase matching). It is worth mentioning that a small residual background spectrum $\varepsilon(\omega)$ may cause overflow in evaluating frequency marginal functions: $\tilde{M}(\omega, \varepsilon) = \tilde{M}(\omega) + \varepsilon(\omega) \times (\int_{-\infty}^{\infty} d\tau)$. Therefore, one has to subtract the spectral background as completely as possible before performing the marginal correction process. Once the standard trace $I_{\text{FROG}}(\omega, \tau)$ has been extracted from the raw data, the well-developed retrieval algorithms [9] can be employed to get solutions for the unknown field. Detailed discussion about the uniqueness of FROG measurements may be found in Ref. [26].

3. Quasi-Phase-Matched LiNbO₃ Waveguides

It is known that second-harmonic power can monotonically increase with interaction length only if the phase velocity (wavevector) mismatch between the

fundamental and second-harmonic waves is canceled. Here we summarize the generalized QPM technique [27,28], which allows for tailoring of phase-matching response to meet specific requirements of applications (such as broad bandwidth in pulsed SHG). We will also discuss the implementation and characterization of our QPM waveguide device, while the experimental demonstration is left in Section 4.

A. Generalized Quasi-Phase-Matching Theory

QPM gratings with strictly periodic nonlinear coefficient distribution $d_{\text{eff}}(z)$ of period Λ_0 can provide an artificial wavevector mK_0 (m is an integer, $K_0 \equiv 2\pi/\Lambda_0$) to compensate for the SHG wavevector mismatch $\Delta k = k(2\omega_0) - 2k(\omega_0)$ at a single fundamental frequency. All the previous formulas remain valid if the constant d_{eff} is substituted by the m th-order Fourier series coefficient of $d_{\text{eff}}(z)$. For aperiodic QPM gratings with a central period Λ_0 , the nonlinear coefficient can be expressed as $d_{\text{eff}}(z) = \tilde{d}_{\text{eff}}(z) \times \exp[-jmK_0z] + \text{c.c.}$, and the baseband phase-matching spectrum (given nondepleted pump and negligible GVD) is generalized to

$$H(\omega) = \int_{-L/2}^{L/2} \tilde{d}_{\text{eff}}(z) e^{-j\zeta z} dz, \quad \text{with } \zeta = -\Delta(v_g^{-1}) \times (\omega - \delta_\omega), \quad (15)$$

where the angular frequency detuning is $\delta_\omega = (mK_0 - \Delta k)/\Delta(v_g^{-1})$. Equation (15) indicates that (i) the central grating period Λ_0 determines the carrier frequency to be phase matched, and (ii) the $H(\omega)$ profile is associated with the “windowed” nonlinear coefficient envelope $\tilde{d}_{\text{eff}}(z) \times \Pi(z/L)$ by Fourier transform, which means there is unique $d_{\text{eff}}(z)$ for each specific complex $H(\omega)$. In practice, the phase-matching spectral phase $\angle H(\omega)$ can be left as a degree of freedom in the design of second-harmonic converters used in intensity autocorrelation and FROG measurements (for they record only the SH pulse energy and power spectrum, respectively). As a result, there exist a number of procedures to approach a specified phase-matching power spectrum $|H(\omega)|^2$ with different designs of $d_{\text{eff}}(z)$ [29–31]. An intuitive way to approach a rectangular $|H(\omega)|^2$ over a broad bandwidth [as in Fig. 1(c)] is by longitudinally changing the QPM period, such that each local period $\Lambda(z)$ can phase match some specific frequency component $\delta_\omega(z) = 2\pi[\Lambda^{-1}(z) - \Lambda_0^{-1}]/\Delta(v_g^{-1})$. Then the overall $H(\omega)$ is the complex superposition of all constituent spectra.

The dotted curve in Fig. 5 illustrates the simulated phase-matching power spectrum $|H(\nu)|^2$ arising from a linearly chirped period function: $\Lambda(z) = \Lambda_0[1 + (\Delta\Lambda/\Lambda_0) \times (z/L)] \times \Pi(z/L)$, where $\Lambda_0 = 14.74 \mu\text{m}$, modulation depth $\Delta\Lambda/\Lambda_0 = 1.85\%$, $L = 59.5 \text{ mm}$, and $\Delta(v_g^{-1}) = -0.37 \text{ ps/mm}$. The resulting PM bandwidth $(\Delta\nu)_{\text{PM}}$ is 6.3 THz, about 150 times that provided by a uniform QPM grating of the same length. The ripple structure of the dotted curve in Fig. 5 is associated with the hard-limited window

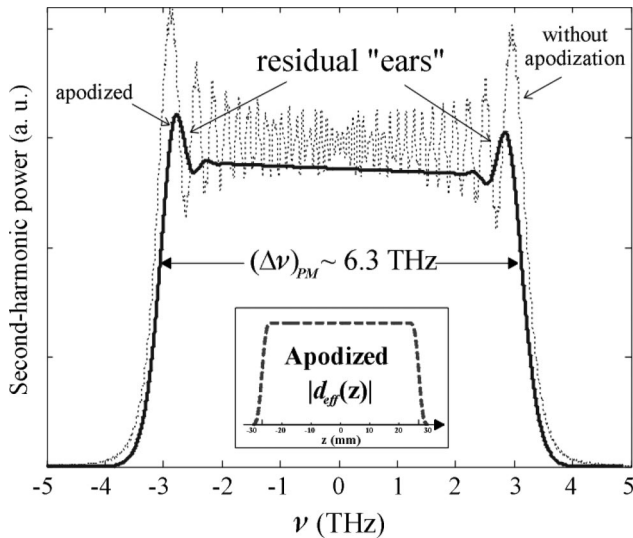


Fig. 5. Simulated baseband phase-matching power spectra using linearly chirped QPM period without (dotted) and with (solid) nonlinear strength apodization. The inset shows the Hamming window function with 10% length used for apodization.

$\Pi(z/L)$ of the nonlinear strength distribution $|d_{\text{eff}}(z)|$, which can be suppressed by multiplying by a spatially apodized window function [32]. For example, the solid curve in the same figure is derived by using a Hamming window function (inset) and a slightly increased modulation depth ($\Delta\Lambda/\Lambda_0 = 2\%$) to compensate the reduced PM bandwidth due to the weaker $|d_{\text{eff}}(z)|$ near the grating edges. It shows improved flatness, while the slight tilt between the residual “ears” is attributed to the nonlinear distribution of wavevector $K(z) = 2\pi/\Lambda(z)$ [though $\Lambda(z)$ is linear]. The “ears” can be eliminated by even stronger apodization at the cost of smaller phase-matching power spectral area A_{PM} . The ripple structure of the phase-matching response only has a weak effect on intensity autocorrelation measurement, for the SH pulse energy $U_{2\omega}$ involves an overlap integral of $|P_{\text{NL}}(\omega)|^2$ and $|H(\omega)|^2$ [Eq. (3)]. In FROG measurements, however, any uneven phase-matching response may distort the measured spectrograms [Eq. (13)]; hence apodization of the nonlinearity amplitude is helpful.

Although chirping the QPM period reduces the phase-matching spectral peak, in the absence of apodization it preserves the power spectral area A_{PM} (available nonlinearity) of the unchirped device. This is because (i) the period function $\Lambda(z)$ simply modulates the phase of nonlinear coefficient envelope, $\tilde{d}_{\text{eff}}(z) = d_{\text{eff}} \times \exp[j2\pi[\Lambda^{-1}(z) - \Lambda_0^{-1}]z]$; (ii) Parseval’s relation results in $A_{\text{PM}} \propto \int_L |\tilde{d}_{\text{eff}}(z)|^2 dz = d_{\text{eff}}^2 L$, which is independent of $\Lambda(z)$. On the contrary, the available nonlinearity is decreased by a factor of N if we use a nonlinear crystal of length L/N to broaden the PM bandwidth by N times: $A_{\text{PM}} \propto \int_{L/N} d_{\text{eff}}^2 dz = d_{\text{eff}}^2 L/N$. Since the second-harmonic yield is proportional to the phase-matching power spectral area (instead of its peak) in the limit where $|P_{\text{NL}}(\omega)|^2$ is

constant, our chirped QPM scheme can produce fundamentally more power in broadband SHG and short pulse measurements, compared to a short crystal with the same bandwidth. Practically, some reduction in SH power will occur when $|P_{\text{NL}}(\omega)|^2$ has spectral rolloff within the transparent band of $|H(\omega)|^2$. However, our previous experiments proved that this reduction in efficiency remains weak if the PM bandwidth remains of the order of the width of nonlinear polarization spectrum [17].

B. Aperiodically Poled Lithium Niobate Waveguide Sample

The A-PPLN waveguide sample used in our experiments was made by electric field poling [33] and annealed proton exchange (APE) [34] in a z -cut LiNbO_3 substrate. The APE process can only increase the extraordinary index ($\Delta n_e \approx 0.09$) and guide TM modes. The size of TM_{00} mode in the fundamental band is made to be $10.7 \mu\text{m}$ wide and $8.2 \mu\text{m}$ deep at the two ends to match single mode fiber (SMF), but is tapered to $8.1 \mu\text{m}$ wide and $4.4 \mu\text{m}$ deep in the QPM grating region to enhance the nonlinear interaction. In view of the coupling and propagation losses ($\sim 0.43 \text{ dB/cm}$ at 1550-nm wavelength), our waveguide sample has a back-to-back loss of $\sim 8.5 \text{ dB}$ (dominated by our free-space coupling). The loss can be significantly reduced to $2\text{--}3 \text{ dB}$ if the waveguide is made by the reverse proton exchange process [35] and is fiber pigtailed [3]. To exploit the largest $\chi^{(2)}$ tensor component of LiNbO_3 ($d_{33} = 27 \text{ pm/V}$), a TM-polarized fundamental beam is coupled into the waveguide to produce a TM-polarized second-harmonic beam. The central poling period Λ_0 is $\sim 14.75 \mu\text{m}$, designed to phase match a fundamental wavelength λ_{PM} of 1538 nm at room temperature. Increasing the sample temperature can shift the central phase-matching wavelength longer (about $0.1\text{--}0.2 \text{ nm/}^\circ\text{C}$) as a result of the effective index change of waveguide modes. The length of the poling region is 5.95 cm , corresponding to a GVM walkoff $T_s \sim 22 \text{ ps}$, since $\Delta(\nu_g^{-1}) \sim -0.37 \text{ ps/mm}$ for the APE waveguides.

The phase-matching tuning curve can be obtained by measuring the output SH power as a function of fundamental wavelength. Figure 6(a) illustrates that an unchirped periodically poled LiNbO_3 (PPLN) waveguide has a sinc^2 tuning curve with a peak response of $\sim 2000 \text{ \%/W}$ and an $\text{FWHM}(\Delta\lambda)_{\text{PM}} \sim 0.17 \text{ nm}$ [i.e., $(\Delta\nu)_{\text{PM}} \sim 42 \text{ GHz}$ in the second-harmonic band], consistent with the 22-ps GVM walkoff. Measurement of subpicosecond pulses with such a PPLN waveguide would be subject to serious distortion [9]. A series of chirped A-PPLN waveguides were fabricated on the same LiNbO_3 sample with different tuning curve widths: $(\Delta\lambda)_{\text{PM}} \sim 5, 10, 15, 20,$ and 25 nm , depending on the modulation depth of the period chirping function. Figure 6(b) shows a phase-matching tuning curve of a chirped A-PPLN waveguide with $(\Delta\lambda)_{\text{PM}} \sim 25 \text{ nm}$ and $(\Delta\nu)_{\text{PM}} \sim 6.3 \text{ THz}$, which is sufficient to accurately

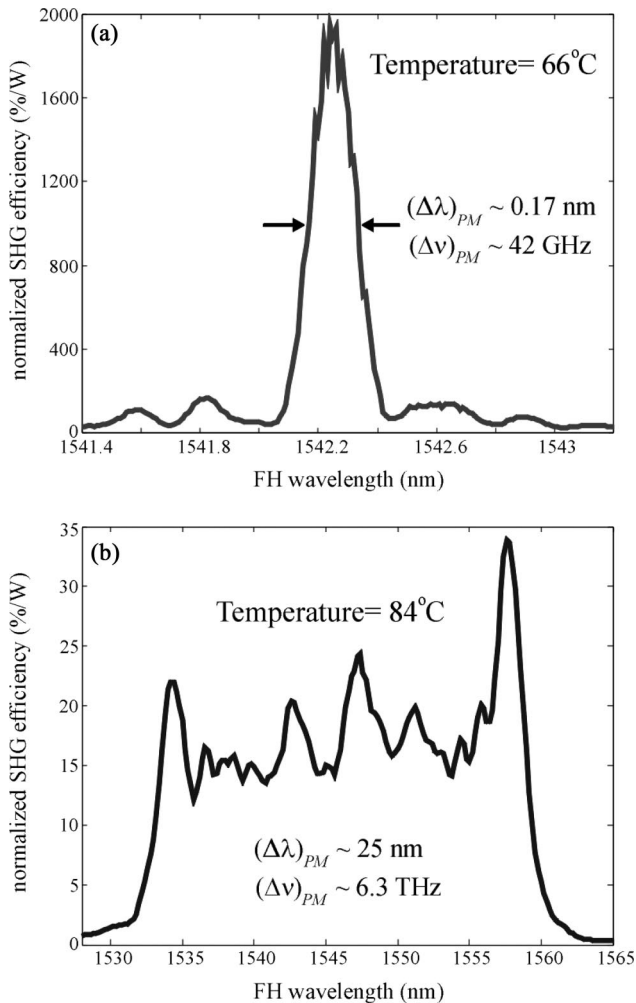


Fig. 6. Measured phase-matching tuning curves of (a) unchirped PPLN waveguide at 66 °C and (b) linearly chirped A-PPLN waveguide at 84 °C. The central phase-matching wavelengths differ by ~ 3 nm due to the 18 °C temperature difference. Note the spectral areas in both cases are roughly the same.

characterize chirp-free pulses with a duration longer than ~ 140 fs. Note that broad PM bandwidth can also be achieved by introducing a thermal gradient on a standard (periodic) QPM grating [36]. However, this scheme is subject to worse coupling stability, has smaller attainable bandwidth, and is difficult to produce specifically specified phase-matching curves. The average efficiency of the curve in Fig. 6(b) is reduced to ~ 15 %/W; however, the spectral area (available nonlinearity A_{PM}) is roughly equal to that of Fig. 6(a). This proves that PM bandwidth broadening by QPM period chirping does not sacrifice the SHG efficiency for short pulses, though the efficiency for continuous waves is indeed reduced. Although we introduced primitive nonlinear strength apodization by tuning the duty cycle of the chirped QPM gratings, the ripple feature [as shown in Fig. 6(b)] persists because (i) only a small portion of QPM grating is apodized, and (ii) the maximum reduction of effective nonlinear coefficient is limited by the minimum domain length achieved by poling technique [32]. As a

result, we still need spectral correction when using A-PPLN waveguides in FROG measurement.

Since the PM bandwidth can be made even wider by increasing the period modulation depth, the minimum measurable pulse duration Δt_{\min} is mainly limited by the GVD-induced input pulse broadening. According to the Sellmeier equation of congruent LiNbO₃ [37], the extraordinary index of refraction near 1.55- μ m wavelength corresponds to a GVD value of ~ 0.1 fs/THz/mm at room temperature. As a result, a 6-cm-long LiNbO₃ waveguide has an accumulated dispersion of ~ 6 fs/THz, which can only slightly broaden the ~ 250 -fs input pulses (spectral width ~ 1.38 THz) used in our experiments. Pulses down to ~ 50 -fs duration at 1.55- μ m wavelength should still be measurable using an appropriately designed 6-cm-long A-PPLN waveguide. However, the minimum pulse duration would be longer for pulses in the visible or near infrared because of the larger GVD (e.g., 0.37 fs/THz/mm at 800-nm wavelength).

4. Experimental Results

A. Autocorrelation Measurement

The experimental setup for autocorrelation measurement is shown in Fig. 2, in which a PPLN or A-PPLN waveguide is employed as the SHG crystal. We used a passively mode-locked fiber laser to generate a 50-MHz, ~ 220 -fs pulse train at 1545-nm wavelength. A Fourier-transform pulse shaper [38] was used to manipulate the complex spectrum in some of the experiments. A collinear Michelson interferometer split and recombined each pulse to form a pulse pair with a variable delay τ with 0.67-fs resolution. The optical beam was made TM polarized before being coupled into the selected waveguide. The sample was heated to 84 °C to shift the central phase-matching wavelength to 1545 nm. The average SH power could be measured by a photomultiplier tube along with a lock-in amplifier down to the order of one femtowatt. The typical data acquisition time for each fringe-resolved autocorrelation trace is less than 3 minutes, where the interferometric fringes and the signal background can be subsequently removed by software to yield the intensity autocorrelation function $G_2(\tau)$.

The record low-power intensity autocorrelation measurement by chirped A-PPLN waveguide was demonstrated in Ref. [17], where the energy per pulse coupled into the waveguide (referring to the total of those from both autocorrelator arms) was only 52 aJ, corresponding to an unprecedented measurement sensitivity of 3.2×10^{-7} mW² (500 times better than the previous record [14]). Here we experimentally demonstrated that insufficient PM bandwidth could distort the autocorrelation traces. Figure 7 illustrates the deconvolved pulse duration Δt (assuming sech² intensity) versus crystal temperature T measured by unchirped PPLN (circle) and chirped A-PPLN (cross) waveguides, respectively. Pulse measurement by PPLN shows strong temperature dependence, where

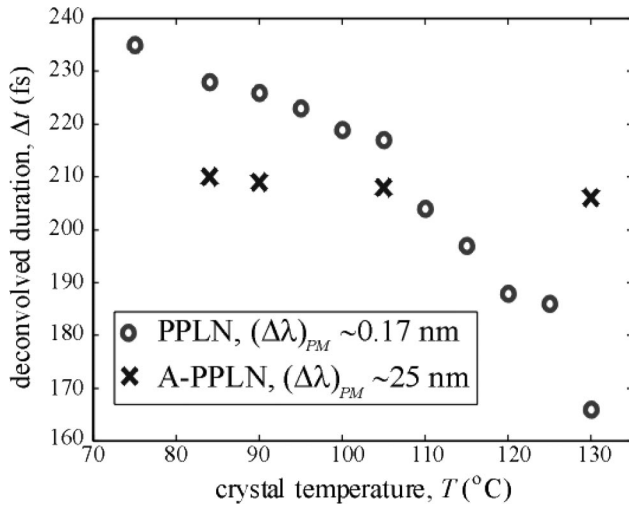


Fig. 7. Deconvolved pulse duration Δt versus crystal temperature T , for unchirped PPLN (circle) and chirped A-PPLN (cross) waveguides.

Δt varies from 235 fs to 166 fs when temperature is increased by 55 °C. In contrast, Δt measured by A-PPLN only varies by a few femtoseconds within the similar temperature range. This is because a narrow phase-matching response $H(\omega)$ cannot sense the entire nonlinear polarization spectrum $P_{NL}(\omega)$, which is essential to retrieve accurate intensity autocorrelation functions. As the central phase-matching wavelength changes with crystal temperature, the narrow $H(\omega)$ of PPLN “samples” different frequency components of $P_{NL}(\omega)$, from which different pulse information and correlation widths are derived. Another demonstration of the importance of adequate PM bandwidth was obtained by measuring nonlinearly chirped Gaussian pulses (created using the pulse shaper) with fixed 9-nm power spectral width (FWHM) and different cubic spectral phases: $\exp[j\gamma \times (\lambda'/9.2 \text{ nm})^3]$, where γ describes the cubic phase strength and $\lambda' = \lambda - 1542 \text{ nm}$ is the wavelength detuning. Figure 8 indicates that the simulated deconvolved pulse duration Δt (assuming infinite PM bandwidth and Gaussian intensity) grows with the increase of γ . Experimental data obtained by a broadband A-PPLN waveguide agree with this trend, where Δt (crosses) varies from 460 fs to 810 fs as γ increases from 0 to 2. Meanwhile, Δt measured by a narrowband PPLN waveguide (circles) is only slightly changed (460 fs \rightarrow 490 fs). This result is a manifestation of the fact that autocorrelation traces acquired with very narrow PM bandwidth are theoretically completely insensitive to odd-order spectral phase (cubic in our experiment). The deviation between the results of simulation and A-PPLN waveguide experiment at large chirp ($\gamma = 2$) could be attributed to (i) an imperfect Gaussian spectrum generated by the shaper, (ii) a finite PM bandwidth, and (iii) a nonflat phase-matching response of the A-PPLN, whose ripples are no longer negligible in measurement of highly chirped pulses.

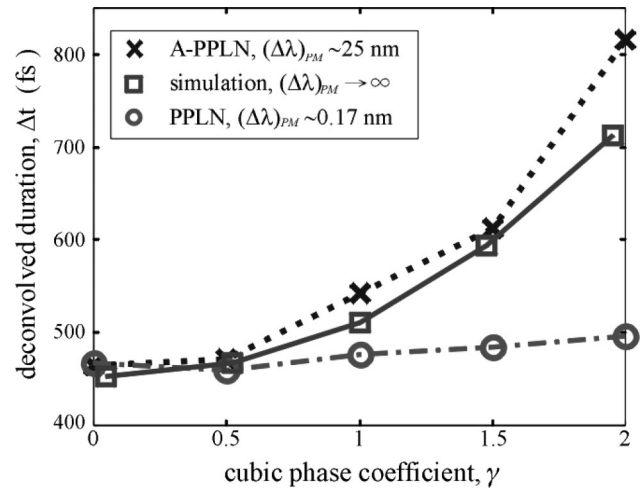


Fig. 8. Deconvolved pulse duration Δt versus cubic spectral phase coefficient γ of a Gaussian spectrum for both PPLN (circle) and A-PPLN (cross) waveguides. The squares show the simulation results.

B. Second Harmonic Generation Frequency-Resolved Optical Gating

The setup of our SHG FROG experiments is shown in Fig. 4, where a chirped A-PPLN waveguide with $(\Delta\lambda)_{PM} \sim 25 \text{ nm}$ is used as the SHG crystal. We employed the same fiber laser and Fourier-transform pulse shaper as those used in the autocorrelation experiments to generate signal pulses at 1538-nm wavelength. The pulse train was sent into a modified collinear Michelson interferometer, giving rise to pulse pairs with variable delay τ . To remove the interferometric fringes by hardware, we use a piezoelectric transducer driven by $\sim 70\text{-Vpp}$, $\sim 180\text{-Hz}$ sinusoidal voltage to dither the fixed arm of the Michelson interferometer by a small displacement d (amplitude $\sim 1.5 \mu\text{m}$). In this way, the SH power spectrum recorded at some delay τ_0 is actually the average of many spectra with slightly different delays $\tau_0 + d\tau$ ($d\tau = 2d/c$). Contrary to the traditional software approach [24], our delay dithering scheme can implement low-pass filtering of interferometric traces without recording and processing a huge amount of data needed to resolve the dense fringes. The output SH power spectrum from the A-PPLN waveguide was recorded by spectrometer and intensified CCD camera as a function of τ , resulting in a fringe-suppressed raw FROG trace $\tilde{I}_{L\text{PF}}(\omega, \tau)$. By moving the variable arm of the Michelson interferometer at a constant speed of $3 \mu\text{m/s}$, and recording one spectrum for every second, we obtained an effective delay resolution $\tau_{\text{res}} = 20 \text{ fs}$. Acquiring a raw FROG trace consisting of 128 spectra takes about 2 minutes. Subsequent software processing deals with (i) background subtraction, (ii) frequency marginal correction [Eq. (14)], and (iii) intensity and phase reconstruction by a commercial software (Femtsoft FROG 3), which normally takes less than one minute to converge.

SHG FROG by use of a chirped A-PPLN waveguide was demonstrated to be able to accurately measure

nearly chirp-free or dispersion stretched pulses at record low power levels, where the corresponding measurement sensitivity is $2.7 \times 10^{-6} \text{ mW}^2$ [18]. Here we further tested the reliability of our A-PPLN waveguide scheme by measuring pulses where the spectral phases were known beforehand. The required signal pulses were created in two different approaches. First, as reported in Ref. [18], we used a 5-meter-long section of single mode fiber (SMF) to broaden the pulse duration by GVD. The retrieved spectral phase profile was in good agreement with that predicted by the fiber dispersion specification. In the second approach, first reported here, we applied a Fourier-transform pulse shaper to impose different cubic spectral phases upon the original pulse train. Figure 9 illustrates the retrieved pulses without [Figs. 9(a)–9(b)] and with [Figs. 9(c)–9(f)] cubic phase modulation in the frequency domain and time domain, respectively. Measurement of modulation-free pulses shows a nearly flat spectral phase [Fig. 9(a)]. In the presence of phase modulation, the retrieved spectral phase profiles in Figs. 9(c) and 9(e) exhibit evident cubic dependence on the wavelength (as well as unimportant linear components). The fitted cubic coefficients are in good agreement with those imposed by the pulse shaper: $0.93 \times 10^{-2} \text{ ps}^3$ ($1.19 \times 10^{-2} \text{ ps}^3$) and $1.90 \times 10^{-2} \text{ ps}^3$ ($2.13 \times 10^{-2} \text{ ps}^3$), respectively. The broadening of the main pulse lobe and the asymmetric oscillatory tails of the temporal intensity profiles shown in Figs. 9(d) and 9(f) are also

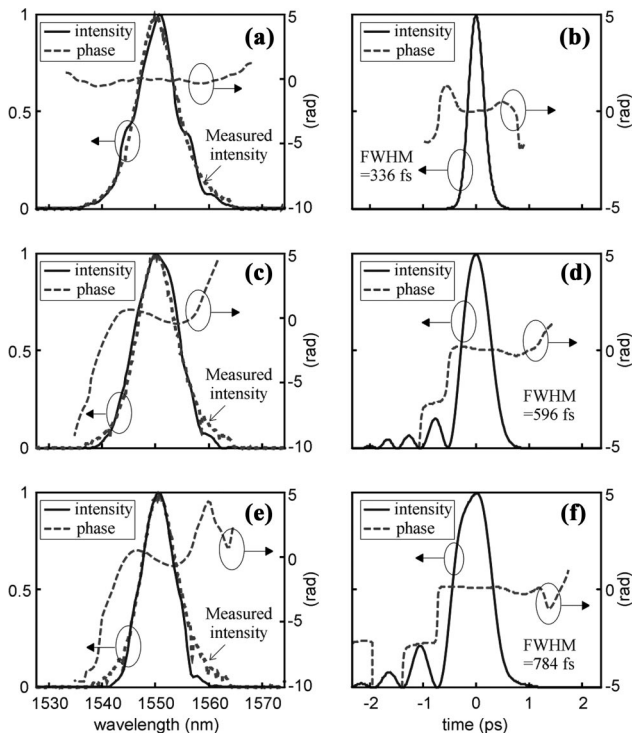


Fig. 9. Retrieved intensity (solid) and phase (dashed) for (a), (b) unchirped and (c)–(f) nonlinearly chirped pulses measured at coupled pulse energy of $\sim 460 \text{ aJ}$. The fitted and imposed cubic spectral phase coefficients in (c) are 0.93×10^{-3} and $1.19 \times 10^{-3} \text{ ps}^3$, while those in (e) are 1.90×10^{-3} and $2.13 \times 10^{-3} \text{ ps}^3$, respectively.

clear signatures of the cubic phase modulation. These measurements directly show that our A-PPLN waveguide scheme can correctly reconstruct the complex field of the unknown pulse with extremely low power requirement.

5. Conclusion

We have examined the theories of SHG, intensity autocorrelation, and interferometric FROG in the presence of different PM bandwidths. Specifically, the analytical form of distorted intensity autocorrelation traces due to a δ -like phase-matching spectrum is proposed for the first time to our knowledge. Experimental intensity autocorrelation and FROG measurement results using A-PPLN waveguides show good data integrity and unprecedented sensitivities of $3.2 \times 10^{-7} \text{ mW}^2$ and $2.7 \times 10^{-6} \text{ mW}^2$, respectively. Further enhancements to our scheme may also be anticipated. For example, apodization of the nonlinear coefficient magnitude $|d_{\text{eff}}(z)|$ in QPM grating design may improve spectral resolution and dynamic range in FROG measurements by suppressing the ripple of the phase-matching spectrum [39]. Fibertailed reverse proton exchange waveguide devices [3,35,39] can achieve even better measurement sensitivity because of the enhanced coupling and nonlinear conversion efficiencies as well as improved coupling stability (longer integration time in detection). Asymmetric Y-junction waveguide devices [40] that are designed to exploit mode sorting to spatially separate the second-harmonic field components arising from the (desired) products of fields from those arising from the (undesired) self-squared terms should be able to realize a noncollinear SHG functionality. If successful, this would eliminate the undesired interferometric fringes (even without delay dithering) and the undesired background signal both in intensity autocorrelation and FROG. We anticipate that the unparalleled ultrashort pulse measurement sensitivity provided by A-PPLN waveguides will substantially contribute to scientific instrumentation, low-power telecommunication signal monitoring, and “optical function generators” when used in conjunction with the pulse shaping techniques.

This work was performed at Purdue University and Stanford University under the support of National Science Foundation grant 0401515-ECS. It was also supported by the National Science Council of Taiwan under grant 95-2112-M-007-018. The authors would like to thank D. E. Leaird for his comprehensive support.

References

1. B. C. Thomsen, D. A. Reid, R. T. Watts, L. P. Barry, and J. D. Harvey, “Characterization of 40-Gbit/s pulses using a lithium niobate modulator at 1550 nm using frequency resolved optical gating,” *IEEE Trans. Instrum. Meas.* **53**, 186–191 (2004).
2. J. P. Ogilvie, D. Débarre, X. Solinas, J. Martin, E. Beaupaire, and M. Joffre, “Use of coherent control for selective two-photon fluorescence microscopy in live organisms,” *Opt. Express* **14**, 759–766 (2006).
3. Z. Jiang, D. S. Seo, S.-D. Yang, D. E. Leaird, R. V. Roussev, C.

- Langrock, M. M. Fejer, and A. M. Weiner, "Four-user, 2.5-Gb/s, spectrally coded OCDMA system demonstration using low-power nonlinear processing," *J. Lightwave Technol.* **23**, 143–158 (2005).
4. N. Belabas and M. Joffre, "Visible-infrared two-dimensional Fourier-transform spectroscopy," *Opt. Lett.* **27**, 2043–2045 (2002).
 5. S. Wielandy, M. Fishteyn, and B. Zhu, "Optical performance monitoring using nonlinear detection," *J. Lightwave Technol.* **22**, 784–793 (2004).
 6. D. N. Fittinghoff, J. L. Bowie, J. N. Sweetser, R. T. Jennings, M. A. Krumbugel, K. W. DeLong, R. Trebino, and I. A. Walmsley, "Measurement of the intensity and phase of ultraweak, ultrashort laser pulses," *Opt. Lett.* **21**, 884–886 (1996).
 7. C. Dorrer and I. Kang, "Real-time implementation of linear spectrograms for the characterization of high bit-rate optical pulse trains," *IEEE Photon. Technol. Lett.* **16**, 858–860 (2004).
 8. J.-Y. Zhang, A. P. Shreenath, M. Kimmel, E. Zeek, R. Trebino, and S. Link, "Measurement of intensity and phase of attojoule femtosecond light pulses using optical-parametric-amplification cross-correlation frequency-resolved optical gating," *Opt. Express* **11**, 601–609 (2003).
 9. R. Trebino, *Frequency-Resolved Optical Gating: the Measurement of Ultrashort Laser Pulses* (Kluwer Academic, 2000).
 10. A. M. Weiner, "Effect of group velocity mismatch on the measurement of ultrashort optical pulses via second harmonic generation," *IEEE J. Quantum Electron.* **19**, 1276–1283 (1983).
 11. J. D. Harvey, J. M. Dudley, D. C. Thomsen, and L. P. Barry, "Ultra-sensitive autocorrelation using two photon absorption," in *Optical Fiber Communications Conference* (Optical Society of America, 1999), Vol. 3, pp. 2–4.
 12. C. Xu, J. M. Roth, W. H. Knox, and K. Bergman, "Ultra-sensitive autocorrelation of 1.5 μm light with single photon counting silicon avalanche photodiode," *Electron. Lett.* **38**, 86–88 (2002).
 13. J. M. Roth, T. E. Murphy, and C. Xu, "Ultrasensitive and high-dynamic-range two-photon absorption in a GaAs photomultiplier tube," *Opt. Lett.* **27**, 2076–2078 (2002).
 14. L. P. Barry, B. C. Thomsen, J. M. Dudley, and J. D. Harvey, "Autocorrelation and ultrafast optical thresholding at 1.5 μm using a commercial InGaAsP 1.3 μm laser diode," *Electron. Lett.* **34**, 358–360 (1998).
 15. P.-A. Lacourt, M. Hanna, and J. M. Dudley, "Broad-band and ultrasensitive pulse characterization using frequency-resolved optical gating via four-wave mixing in a semiconductor optical amplifier," *IEEE Photon. Technol. Lett.* **17**, 157–159 (2005).
 16. P.-A. Lacourt, J. M. Dudley, J.-M. Merolla, H. Porte, J.-P. Goedgebuer, and W. T. Rhodes, "Milliwatt-peak-power pulse characterization at 1.55 μm by wavelength-conversion frequency-resolved optical gating," *Opt. Lett.* **27**, 863–865 (2002).
 17. S.-D. Yang, A. M. Weiner, K. R. Parameswaran, and M. M. Fejer, "400-photon-per-pulse ultrashort pulse autocorrelation measurement with aperiodically poled lithium niobate waveguides at 1.55 μm ," *Opt. Lett.* **29**, 2070–2072 (2004).
 18. S.-D. Yang, A. M. Weiner, K. R. Parameswaran, and M. M. Fejer, "Ultra-sensitive frequency-resolved optical gating by aperiodically poled LiNbO₃ waveguides at 1.5 μm ," *Opt. Lett.* **30**, 2164–2166 (2005).
 19. R. W. Boyd, *Nonlinear Optics* (Academic, 1992).
 20. A. M. Weiner, *Ultrafast Optics* (Wiley, 2007).
 21. E. P. Ippen and C. V. Shank, "Techniques for measurement," in *Ultrashort Light Pulses: Picosecond Techniques and Applications*, S. L. Shapiro, ed. (Springer-Verlag, 1977), Vol. 18.
 22. S.-D. Yang and Y.-Y. Huang, "Even-order spectral phase retrieval by modified interferometric field autocorrelation trace," to be presented at the 20th Annual Meeting of the IEEE Lasers and Electro-Optics Society, Lake Buena Vista, Fla., 21–25 October 2007.
 23. J. Prawiharjo, F. Parmigiani, K. Gallo, P. Petropoulos, N. G. R. Broderick, and D. J. Richardson, "Cascaaded $\chi^{(2)}$ interaction based frequency-resolved optical gating in a periodically-poled LiNbO₃ waveguide," *Opt. Lett.* **31**, 244–246 (2006).
 24. G. Stibenz and G. Steinmeyer, "Interferometric frequency-resolved optical gating," *Opt. Express* **13**, 2617–2626 (2005).
 25. G. Taft, A. Rundquist, M. M. Murnane, I. P. Christov, H. C. Kapteyn, K. W. DeLong, D. N. Fittinghoff, M. A. Krumbugel, J. N. Sweetser, and R. Trebino, "Measurement of 10-fs laser pulses," *IEEE J. Sel. Top. Quantum Electron.* **2**, 575–585 (1996).
 26. B. Seifert, H. Stolz, and M. Tasche, "Nontrivial ambiguities for blind frequency-resolved optical gating and the problem of uniqueness," *J. Opt. Soc. Am. B* **21**, 1089–1097 (2004).
 27. M. M. Fejer, G. A. Magel, D. H. Jundt, and R. L. Byer, "Quasi-phase-matched second harmonic generation: tuning and tolerances," *IEEE J. Quantum Electron.* **28**, 2631–2654 (1992).
 28. G. Imeshev, M. A. Arbore, M. M. Fejer, A. Galvanauskas, M. Fermann, and D. Harter, "Ultrashort-pulse second-harmonic generation with longitudinally nonuniform quasi-phase-matched gratings: pulse compression and shaping," *J. Opt. Soc. Am. B* **17**, 304–318 (2000).
 29. M. H. Chou, K. R. Parameswaran, and M. M. Fejer, "Multiple-channel wavelength conversion by use of engineered quasi-phase-matching structures in LiNbO₃ waveguides," *Opt. Lett.* **24**, 1157–1159 (1999).
 30. Y. W. Lee, F. C. Fan, Y. C. Haung, B. Y. Gu, B. Z. Dong, and M. H. Chou, "Nonlinear multiwavelength conversion based on aperiodic optical superlattice in lithium niobate," *Opt. Lett.* **27**, 2191–2193 (2002).
 31. C. R. Fernández-Pousa and J. Capmany, "Dammann grating design of domain-engineered lithium niobate for equalized wavelength conversion grids," *IEEE Photon. Technol. Lett.* **17**, 1037–1039 (2005).
 32. J. Huang, X. P. Xie, C. Langrock, R. V. Roussev, D. S. Hum, and M. M. Fejer, "Amplitude modulation and apodization of quasi-phase-matched interactions," *Opt. Lett.* **31**, 604–606 (2006).
 33. L. E. Myers, R. C. Eckardt, M. M. Fejer, R. L. Byer, W. R. Bosenburg, and J. W. Pierce, "Quasi-phase-matched optical parametric oscillators in bulk periodically poled LiNbO₃," *J. Opt. Soc. Am. B* **12**, 2102–2116 (1995).
 34. K. R. Parameswaran, J. R. Kurz, R. V. Roussev, and M. M. Fejer, "Observation of 99% pump depletion in single-pass second-harmonic generation in a periodically poled lithium niobate waveguide," *Opt. Lett.* **27**, 43–45 (2002).
 35. K. R. Parameswaran, R. K. Route, J. R. Kurz, R. V. Roussev, M. M. Fejer, and M. Fujimura, "Highly efficient second-harmonic generation in buried waveguides formed by annealed and reverse proton exchange in periodically poled lithium niobate," *Opt. Lett.* **27**, 179–181 (2002).
 36. Y. L. Lee, Y.-C. Noh, C. Jung, T. J. Yu, D.-K. Ko, and J. Lee, "Broadening of the second-harmonic phase-matching bandwidth in a temperature-gradient-controlled periodically poled Ti:LiNbO₃ channel waveguide," *Opt. Express* **11**, 2813–2819 (2003).
 37. D. H. Jundt, "Temperature-dependent Sellmeier equation for the index of refraction, n_e , in congruent lithium niobate," *Opt. Lett.* **22**, 1553–1555 (1997).
 38. A. M. Weiner, "Femtosecond pulse shaping using spatial light modulators," *Rev. Sci. Instrum.* **71**, 1929–1960 (2000).
 39. H. Miao, A. M. Weiner, C. Langrock, R. V. Roussev, and M. M. Fejer, "Polarization-insensitive ultralow-power second-harmonic generation frequency-resolved optical gating," *Opt. Lett.* **32**, 874–876 (2007).
 40. J. R. Kurz, J. Huang, X. Xie, T. Saida, and M. M. Fejer, "Mode multiplexing in optical frequency mixers," *Opt. Lett.* **29**, 551–553 (2004).